energies

MDPI

Article

Electromagnetic Characterization of Silicon–Iron Additively Manufactured Cores for Electric Machines

Daniele Michieletto [1], Luigi Alberti [1,*], Filippo Zanini [2] and Simone Carmignato [2]

[1] Department of Industrial Engineering, University of Padova, 35131 Padova, Italy; daniele.michieletto@phd.unipd.it

[2] Department of Management and Engineering, University of Padova, 36100 Vicenza, Italy; filippo.zanini@unipd.it (F.Z.); simone.carmignato@unipd.it (S.C.)

* Correspondence: luigi.alberti@unipd.it

Abstract: This paper deals with the electromagnetic characterization of a laminated toroidal ferromagnetic core made through additive manufacturing, specifically using the laser powder bed fusion process. The continuing demand for increasingly efficient, lightweight, and higher performance electric machines is creating huge challenges in the design and realization of new electric motor solutions. The constant improvements in additive manufacturing technologies have prompted researchers to investigate the possibility of adopting these production techniques for the manufacture of high-value electric motors. For these reasons, this paper investigates the ferromagnetic characteristics of an additively manufactured core made with FeSi6.5 powder. The BH curve and the specific iron losses of the processed material have been measured so that they can be compared with a commercial lamination, and have the possibility of carrying out more precise finite element simulations.

Keywords: additive manufacturing; laser powder bed fusion; FeSi6.5; electric drives; electric motors; synchronous motors; soft magnetic materials; magnetic characterization; printed laminated cores

Citation: Michieletto, D.; Alberti, L.; Zanini, F.; Carmignato, S; Electromagnetic Characterization of Silicon–Iron Additively Manufactured Cores for Electric Machines. *Energies* **2024**, *17*, 650. https://doi.org/10.3390/en17030650

Academic Editor: Yacine Amara

Received: 1 December 2023
Revised: 24 January 2024
Accepted: 26 January 2024
Published: 30 January 2024

1. Introduction

In recent years, the demand for even more high-performance components is increasing day by day for many reasons. For example, climate change [1,2] and zero-emission aims [3–5] are stimulating several industrial sectors to move toward the electrification and energy efficiency of their products. To achieve this goal, innovative solutions are being experimented on, including additive manufacturing (AM) [6–15], also called 3D printing. This new manufacturing method allows high-value components to be produced with a wider degree of freedom in the design process. A vast variety of complex geometric shapes can be made, as long as the practical limits of the AM machine are not exceeded [16,17]. Moreover, it is possible to achieve significant volume production of components through AM. This is further supported by the fact that some aerospace companies have already declared the integration of AM into their production processes [18,19].

Because of its promising characteristics, AM has attracted attention from the perspective of electric machine manufacturing. However, unlike traditional manufacturing methods, the AM process has not reached an advanced stage for electric machines. In any case, with continued advances in the field of AM, it is poised to emerge as an alternative for the production of electric machines. This is due to the flexibility of the design possibilities offered by AM, which allows the integration of structural and thermal management components with active parts, making it the optimal solution for various applications.

From a design and manufacturing perspective, any electrical machine can be divided into several subcomponents, such as the ferromagnetic core, coils/winds, permanent magnets, thermal management components, and the mechanical apparatus.

The windings, consisting of coils, insulating material, and supports, are critical to generate the magnetic field inside the electrical machine. From the perspective of electrical machine design and construction, it is essential to minimize the power losses of this component to improve the efficiency of the electrical machine and avoid overheating problems. Therefore, low electrical resistivity should be pursued. However, in modern machine applications requiring high-speed and high-frequency operation, problems arise due to the predominance of losses associated with skin and proximity effects, which complicate the design of the winding assembly. Traditional design and manufacturing techniques often struggle to maintain a balance between these crucial factors. The adoption of AM for the production of new types of windings has been studied, demonstrating how windings can be made to meet multiple requirements, from improving the resistivity of materials to reducing high-frequency losses and finally to thermal dissipation [20–22].

Machines that emphasize efficiency, compactness and high torque-to-weight ratio use permanent magnets. Consequently, the manufacturing process and the resulting PM properties are of fundamental importance in these applications. Also in this area, AM has been considered and used for the production of magnets. Several production processes have been studied and have provided promising results for the production of high-performance magnets [23–26].

Mechanical and structural components are also being considered for production using additive manufacturing (AM) techniques, giving designers and electrical machine manufacturers the opportunity to reconsider the design of these components. The wide range of material options and design freedom make it easier to reduce the size and weight of structural parts through the use of different lattice structures. In addition, AM allows the integration of various features that conventional manufacturing techniques cannot achieve. This results in the creation of more compact, high power density, low inertia electrical machines without compromising reliability. Different example of these applications, as for example heat exchangers and various potential options for structural topologies, have been presented in [27,28].

The core of an electrical machine is a high-permeability magnetic structure used to confine and direct the magnetic field. When thinking about its design and construction, several magnetic properties must be considered, including magnetic saturation, permeability, hysteresis losses, and eddy current losses. The possibility of realizing complex magnetic geometries by using AM techniques would allow new motor structures to be designed and investigated with the aim of improving their performance. However, it is necessary that the printed core presents good magnetic properties, comparable to those of a commercial lamination. The electromagnetic characteristics of the material obtained by using AM processes are fundamental, so several specific specimens were fabricated and tested in the literature to measure the magnetic properties of the printed material and to verify their relation to the process parameters used to produce them (e.g., power and speed of the laser, hatch distance, and layer thickness) and the composition of the powder. The most widely used geometric shape in the literature for this purpose is a solid toroid. Different powder compositions have been studied: pure iron [29], FeSi3.7 [30], Fe91Si9 [31], FeSi4 [32], FeSi6.7 [33], and FeSi2.9 [34]. Instead of producing a solid toroid, a laminated toroidal sample has been chosen in this work to fine-tune the AM process for laminated structures, and to characterize the magnetic behavior and measure the iron losses. In current manufacturing processes for metal sheets, a high silicon content can lead to several production and technical problems, prompting manufacturers to use compositions that do not exceed 4 % of silicon. Some of the problems associated with high silicon content include the following [35–38]:

- Fragility of Material: Increased silicon content can make ferromagnetic sheets more brittle. This can lead to difficulties when processing and handling the sheets.
- High Production Costs: The introduction of high silicon content can result in higher production costs due to the need for more sophisticated machinery and processes to ensure the desired quality of the material.

- Weldability Issues: High silicon content can affect the weldability of sheets. Welding of materials with high silicon content may require additional attention and special techniques to avoid the formation of defects in welded joints.

All these problems can be overcome in AM processes by fine-tuning the printing parameters to produce ready-to-use components that require limited post-processing. This study is a first investigation needed to enable the development of new electrical machines, as for example the synchronous reluctance motor presented in [39–41]. The knowledge of the BH curve of the printed material and its losses will allow more accurate simulations to be performed, while the optimization of the AM process parameters will permit laminated magnetic cores able to satisfy the various technical requirements demanded by the motor to be realized.

The paper is divided into four main sections. The first one provides a detailed explanation of how the toroid was manufactured, including information about the materials used, the production process, and features. The goal is to provide the reader with a clear understanding of the toroid's manufacturing process and the specific factors which can influence its properties and performance.

The second section includes information about the toroid's magnetic properties and its behavior under different conditions. In particular, the BH curve of the AM material and its power losses are presented in detail.

The third section focus on a specific application of the AM toroid presented in the paper. It describes how the characterization of the magnetic properties of the AM material are used within the design and analysis of electric machines. Moreover, some experimental measurements on an actual AM synchronous reluctance rotor are shown.

Finally, the last section summarizes the key findings and implications of the research.

2. Description of the Manufacturing Process

The AM process used in this work is laser powder bed fusion (L-PBF) [42–44]. This process consists in melting selectively the powder with a layer-by-layer approach, so as to obtain an object with complex geometry that would be difficult to produce with traditional manufacturing processes. The L-PBF process can be split into three main parts:

1. The realization of a CAD model of the specimen to be produced;
2. The manufacturing process itself;
3. The post-process operations to finalize the sample.

The L-PBF manufacturing process consists in spreading consecutive thin layers of powder with a coater over the build platform and melting the powder with a laser following the CAD model. The powder tank is raised by one layer thickness while the build platform is lowered by the same amount at each iteration. The process is repeated until the component is finished. Figure 1 shows the L-PBF machine (i.e., SISMA MySint100 [45]) used during the fabrication of the specimen.

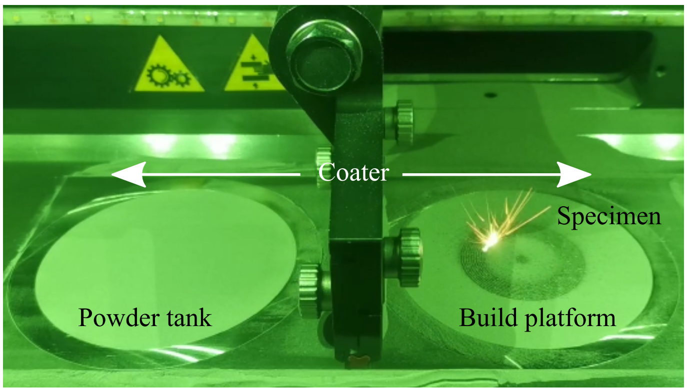

Figure 1. Laser powder bed fusion process.

In this work a commercial silicon/iron powder (supplier: Höganäs [46]) was used to realize all the samples. The silicon percentage was equal to 6.5 % (FeSi6.5) to exploit the advantages that high-silicon powders provide. The addition of silicon to iron allows the electrical resistivity of the alloy to be increased, reducing losses due to hysteresis and eddy currents when the material is subjected to varying magnetic fields [47–50]. On the other hand, the presence of silicon affects the ferromagnetic properties of the alloy. Therefore, a compromise percentage of silicon was chosen to achieve good magnetic properties and low ferromagnetic losses.

Powder characterization was carried out using X-ray computed tomography (Nikon Metrology MCT225 [51]). This technology enables three-dimensional analysis, characterizing the size and shape of particles. The powders were placed in a cylindrical container with a diameter of 5 mm to obtain high-resolution scans and facilitate the analysis of a large number of particles. The obtained results are reported in Table 1.

Before fabricating the laminated toroid, the L-PBF process parameters were optimized by producing dedicated specimens (maximum thickness equal to 1 mm) using different combinations of parameters, with the aim of reducing the presence of defects (porosity and cracks) and avoiding classic problems associated with this type of technology, such as keyhole [52–55] or lack of fusion [56–59], for better quality and magnetic performance of the final components. In particular, laser power, laser speed, and hatch distance were varied to obtain different energy densities from 58 to 159 J/mm^3. The best parameter setup was identified based on the achieved relative density, which is typically reduced in L-PBF parts by the intrinsic presence of internal closed pores. For this reason the printing process was mainly optimized to minimize the presence of hollow spaces inside the material but also considering all the other problems listed so far.

Table 1. Powder particle morphology.

Min. dimension [µm]	Max. dimension [µm]	Avg. dimension [µm]
3.72	59.3	27.7
D10 [µm]	D50 [µm]	D90 [µm]
18.7	27.2	37.5

The specimens density was measured using the Archimedes method [60]. This technique consists in weighing the sample in air and in a fluid, and applying the following formula:

$$\rho = \frac{m_a}{m_a - m_{fl}} \rho_{fl} \tag{1}$$

where ρ_{fl} is the density of the fluid, m_a is the mass of the sample in air (equal to 1.5968 g), and m_{fl} is the mass of the sample in the fluid (equal to 1.3812 g). The fluid used in this case was pure water $\left(\rho_{fl} = 1\,\mathrm{g/cm^3}\right)$. The density of the AM material was 7.4038 g/cm^3. The porosity, ϕ, of the specimens was calculated considering the reference density of a standard FeSi6.5 alloy equal to 7.48 g/cm^3 and it was equal to 1.02 %.

The final optimized parameters, corresponding to the lowest achieved porosity content (i.e., 0.91 %) were laser powder 125 W, speed 750 mm/s, hatch distance 0.08 mm, and layer thickness 0.02 mm. Based on the density achieved using the optimized process parameters, the ferromagnetic mass of the toroidal sample was estimated to be equal to 46 g.

3. Characterization of the Toroid

The BH curve of the magnetic material is a key aspect to obtain motors with high performance. The knowledge of this property allows both new magnetic materials to be compared with the existing ones and more accurate finite element analyses to be performed. For this reason, a laminated toroidal specimen, shown in Figure 2, was realized by L-PBF using the optimized process parameters to characterize the magnetic behavior of the additively manufactured material. The windings are distributed regularly all around the circumference, as show in Figure 2b, in order to produce a more uniform magnetic field distribution and improving the mutual coupling between the coils. The sample consists of 10 equally spaced concentric ferromagnetic paths with a total area equal to 50 mm^2 and a mean magnetic path of 124.1 mm. In the hollow spaces, resin was inserted after the L-PBF process to hold the printed material together. Figure 3 shows a cross-section of the specimen with its main dimensions.

For the measurement of the electromagnetic characteristics, a state-of-the-art procedure, i.e., Ref. [61], has been adopted. The circuit used for the measurements is reported in Figure 4. A controlled AC source is utilized to vary the frequency and the maximum current during the measurements. The other quantities of interest are achieved by post-elaboration.

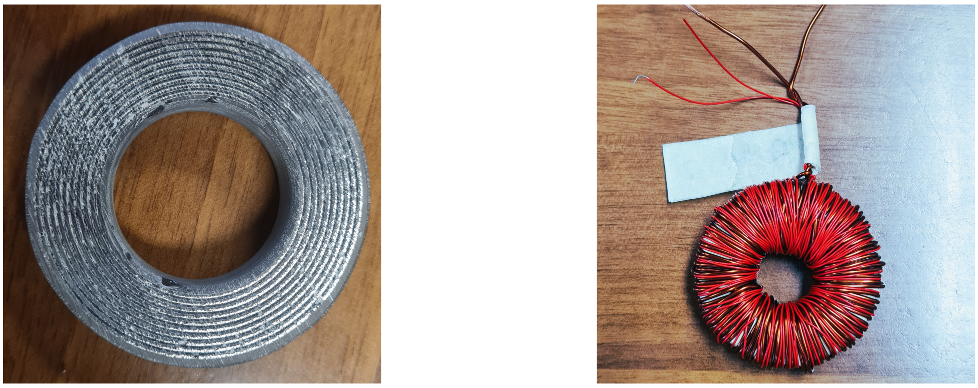

(**a**) Ferromagnetic core (**b**) Wound sample

Figure 2. Laminated toroidal specimen produced by L-PBF.

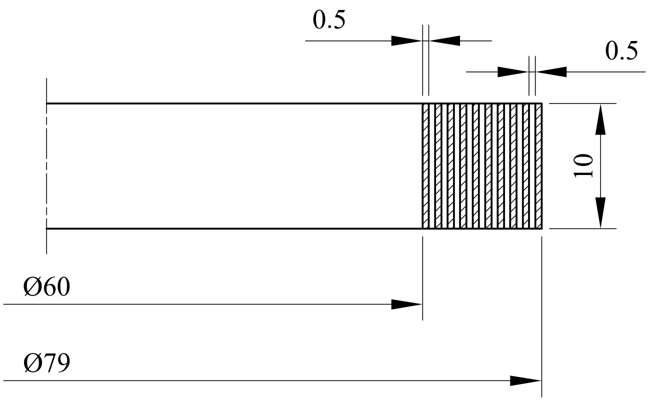

Figure 3. Cross-section of the toroidal specimen. Dimensions in millimeters.

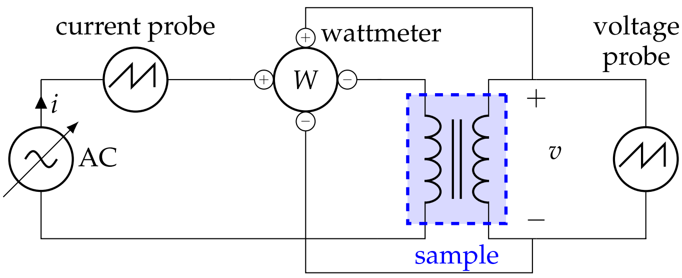

Figure 4. Measurement circuit.

3.1. BH Curve

The BH curve of the toroidal specimen can be obtained elaborating the signals of current and voltage probes of Figure 4. As an example, Figure 5 shows the waveforms for a supply frequency of 50 Hz. The resulting BH loops are reported in Figure 6 where different current levels are considered as well. From each BH loop, the peak value of the magnetic field and the associated flux density can be extracted so as to create the BH curve of the printed material. Figure 7 shows the effects of process parameters on the magnetic properties of the printed material. All the BH curves are computed considering the same sample geometry and powder composition but using different parameters during the manufacturing process. It can be noticed that the printing parameters strongly affect the magnetic properties of the material. This is due to the different microstructures created within the printed material, so they need to be chosen carefully. In Figure 8, the measured BH characteristic is compared with that of a commercial lamination with a silicon content of 3 % and a thickness equal to 0.5 mm [62]. Moreover, the characteristics of the printed material presented in [34] are also included in the comparison. The powders considered in this work (FeSi6.5) and in [34] (FeSi2.9) are different, as well as the process parameters, so different material performances are expected. Therefore, the found discrepancy is reasonable. It can be noted that the proposed FeSi6.5 specimen exhibits a slightly worse performance behavior compare to the FeSi2.9 specimen in the first part of the BH curve but shows higher values of flux density when the material starts to saturate, even for relatively low magnetic fields (around 3–4 kA/m). The proposed FeSi6.5 sample has a BH characteristic very similar to the reference lamination, especially for high magnetic fields.

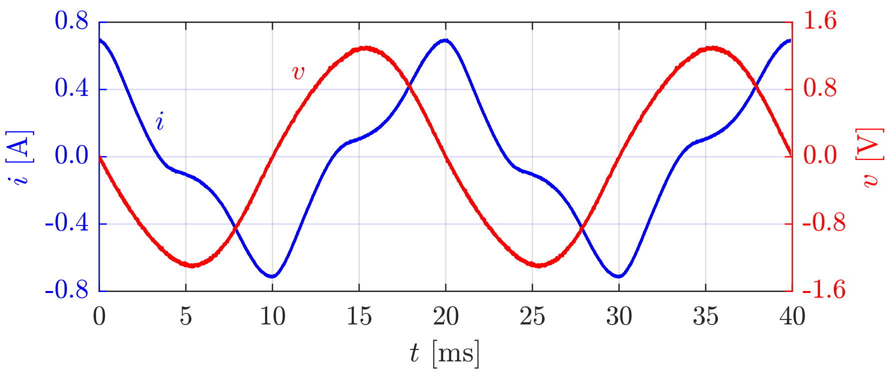

Figure 5. Current and voltage waveform examples. Power supply frequency: 50 Hz.

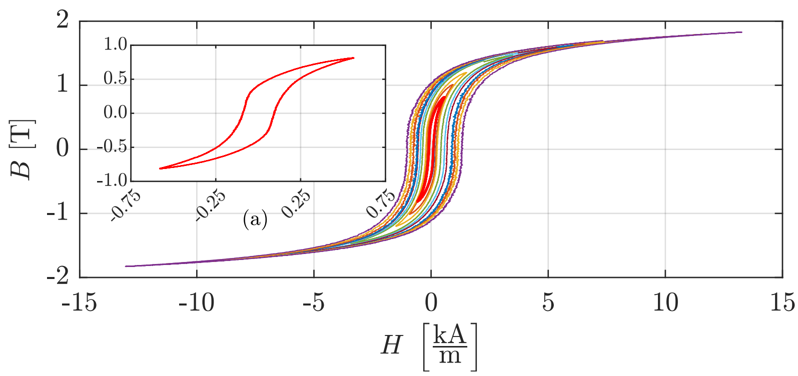

Figure 6. BH loops for different values of magnetic field intensity. Power supply frequency: 50 Hz.

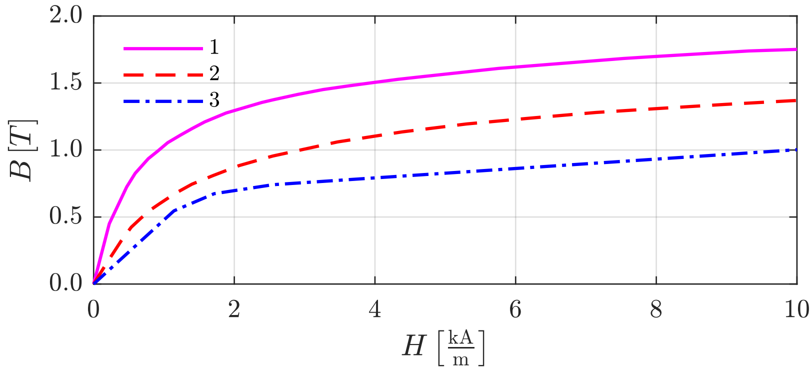

Figure 7. BH curves of the printed material manufactured with different printing parameters. 1—Laser powder: 125 W, speed: 750 mm/s, hatch distance: 0.08 mm, layer thickness: 0.02 mm. 2—Laser powder: 125 W, speed: 700 mm/s, hatch distance: 0.09 mm, layer thickness: 0.02 mm. 3—Laser powder: 120 W, speed: 800 mm/s, hatch distance: 0.09 mm, layer thickness: 0.03 mm.

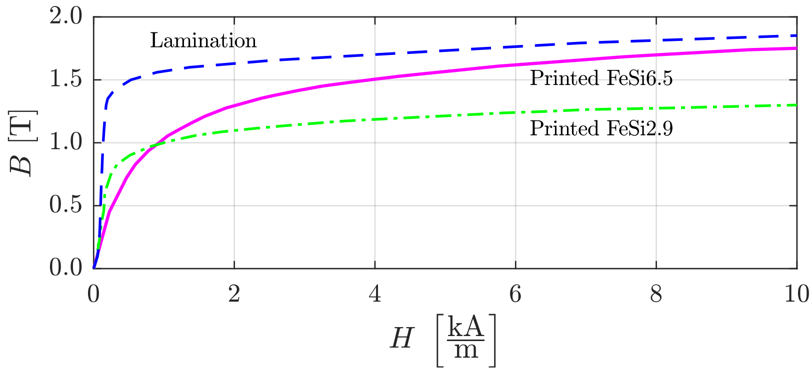

Figure 8. BH curves of ferromagnetic materials obtained with different manufacturing processes.

3.2. Power Losses

Power losses are measured using the wattmeter shown in Figure 4. This quantity is strictly connected to the specimen dimension so the specific iron losses p_{ir} will be considered hereafter. The iron losses are affected by the flux density intensity at which the ferromagnetic material works and by the operating frequency. To have a comprehensive idea of the iron losses, several experimental tests have been carried out varying the frequency of the power supply and the current amplitude. Figure 9 shows the experimental results obtained. The specific power losses can be analytically computed as a function of the flux density B and the supply frequency f using the following equation based on the Steinmetz formula:

$$p_{ir}(B,f) = \left(\frac{B}{B^*}\right)^2 \left(\frac{f}{f^*}\right) \left[p_{ist} + p_{ec}\left(\frac{f}{f^*}\right)\right] \tag{2}$$

where p_{ist} and p_{ec} represent the hysteresis and eddy currents specific losses, while B^* and f^* are assumed equal to 1 T and 50 Hz, respectively, as for the usual ferromagnetic data sheet. Fitting the measured losses with Equation (2) allows the following values to be computed for p_{ist} and p_{ec}; this permits the losses to be expressed with good accuracy in the considered current-frequency range.

$$p_{ir}(B,f) = B^2 \left(\frac{f}{50}\right) \left[2.392 + 0.208\left(\frac{f}{50}\right)\right] \tag{3}$$

Figure 9 shows the specific iron losses computed with Equation (3) (solid line) as a function of the flux density for the different frequencies considered during the measurements. Figure 10 shows the BH loops for different frequencies of the power supply. The area inside the BH loop grows with the increase in the frequency as expected, since it is proportional to the total iron losses.

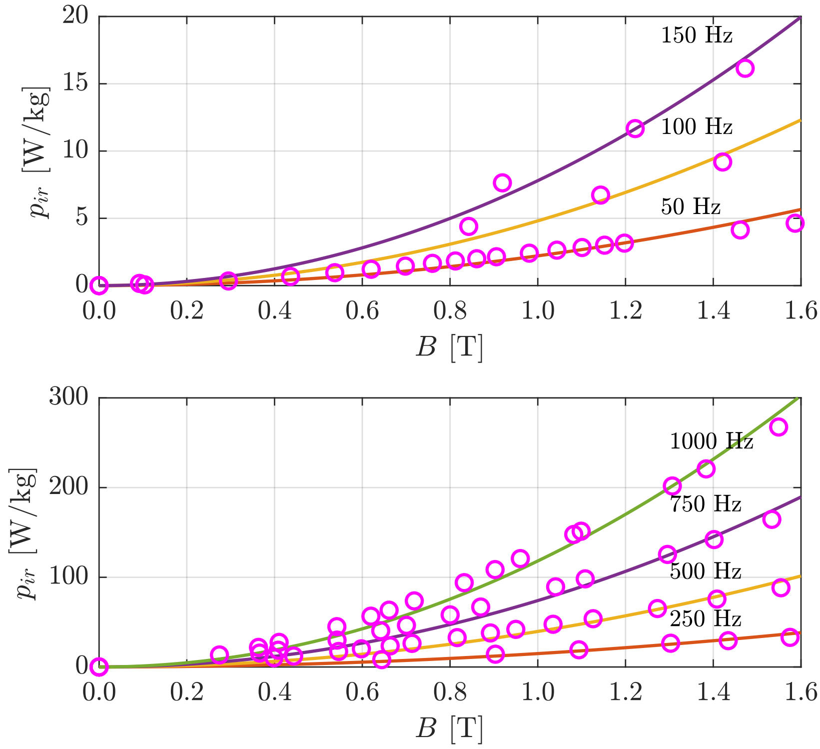

Figure 9. Experimental measurements (circles) and analytical model prediction (solid lines).

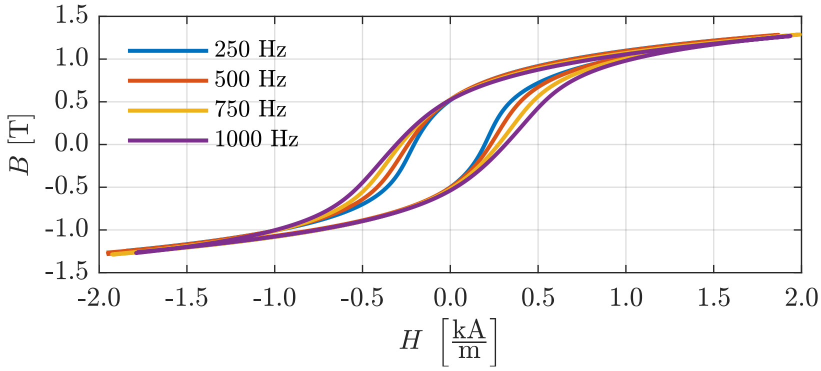

Figure 10. BH loop with different power supply frequencies.

4. Application Example: Synchronous Reluctance Motor Magnetic Characteristic

As an application example, the magnetic characteristics of a synchronous reluctance motor with additively manufactured rotor are presented in this section. A preliminary design and analysis of the considered machine has been carried out in [39]. Using the experimental measurements obtained in the previous sections, it is possible to perform accurate finite element simulations [63] of the magnetic characteristics of the motor which are a key aspect to calculate the motor performance, since the torque of the electric machine can be computed as $3/2p\left(\Lambda_d I_q - \Lambda_q I_d\right)$ where p is the number of pole pairs, Λ_d is the direct flux linkage, and Λ_q is the quadrature flux linkage while I_d and I_q are the feed currents of the two axes. Figure 11 shows a cross-section of the lamination. The stator is formed by reference lamination (see also the characteristic of Figure 8) while for the rotor the BH curve measured on the sample of Figure 2 has been adopted. The flux linkages can be calculated by integrating the vector magnetic potential over the stator slots. For a generic jth phase ($j = a, b, c$) the formula is as follows:

$$\Lambda_j = \sum_{i=1}^{Q_{sim}} \frac{Q_s}{Q_{sim}} \frac{n_c k_j(i)}{n_{pp} S_{slot}} \int_{S_{slot}} A_z dS_{slot} \quad (4)$$

where A_z is the vector magnetic potential, $k_j(i)$ is a coefficient which represents the filling of the ith slot by the conductors of the jth phase, Q_{sim} is the number of simulated slots, S_{slot} is the cross-area section of the slot, n_c is the number of conductors in the slot, and n_{pp} the number of the winding parallel paths. Once the flux linkages Λ_a, Λ_b, and Λ_c are obtained, the flux linkages Λ_d and Λ_q can be computed using the Clarke–Park transformation (5) and (6) where ϑ_m is the rotor mechanical position.

$$\Lambda_d = \frac{2}{3}\left[\Lambda_a \cos(\vartheta_m) + \Lambda_b \cos\left(\vartheta_m - \frac{2}{3}\pi\right) + \Lambda_c \cos\left(\vartheta_m + \frac{2}{3}\pi\right)\right] \quad (5)$$

$$\Lambda_q = -\frac{2}{3}\left[\Lambda_a \sin(\vartheta_m) + \Lambda_b \sin\left(\vartheta_m - \frac{2}{3}\pi\right) + \Lambda_c \sin\left(\vartheta_m + \frac{2}{3}\pi\right)\right] \quad (6)$$

Figure 11b shows an example of the flux lines when only the d-axis of the motor is excited. Figure 12a shows the rotor obtained from the printing process described in the previous sections, while Figure 12b,c show the test bench, the measurement system, and the assembled motor ready to be tested. The prototype is rotated at a constant speed and supplied with different current values. By means of voltage probes, the phase voltages are measured from which, knowing the rotational speed of the motor, the flux linkages are calculated. Figure 13 shows the simulated and measured flux linkage of the motor. It is worth noticing the good agreement between the simulations and measurements thanks to the accurate characterization of the printed material adopted in the rotor.

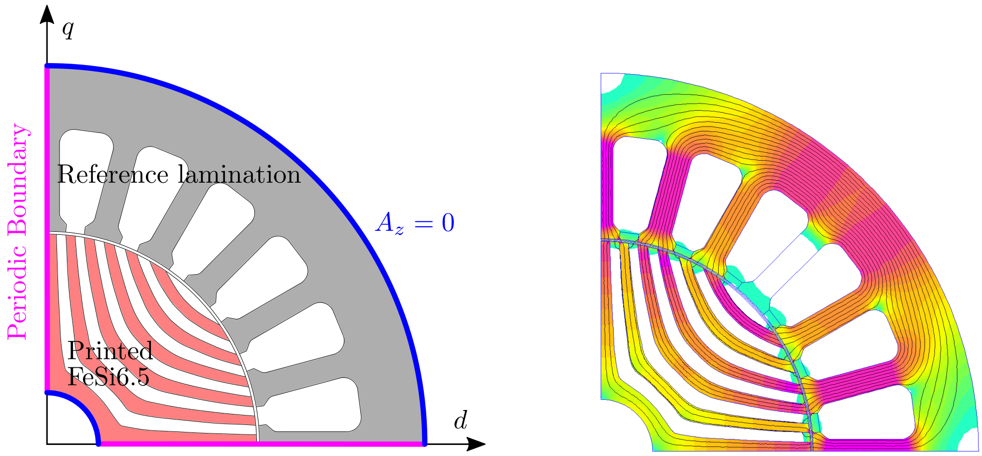

(**a**) Ferromagnetic materials of stator and rotor (**b**) Finite element analysis

Figure 11. Synchronous reluctance motor with printed rotor, finite element model.

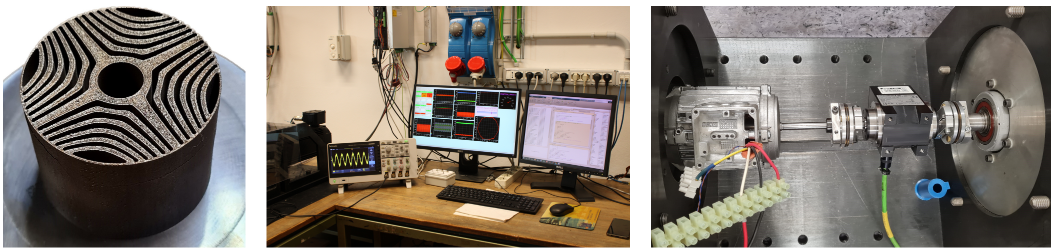

(**a**) Printed sample (**b**) Measurement system (**c**) Prototype assembled on the test bench

Figure 12. Synchronous reluctance rotor fabricated with AM process and test bench.

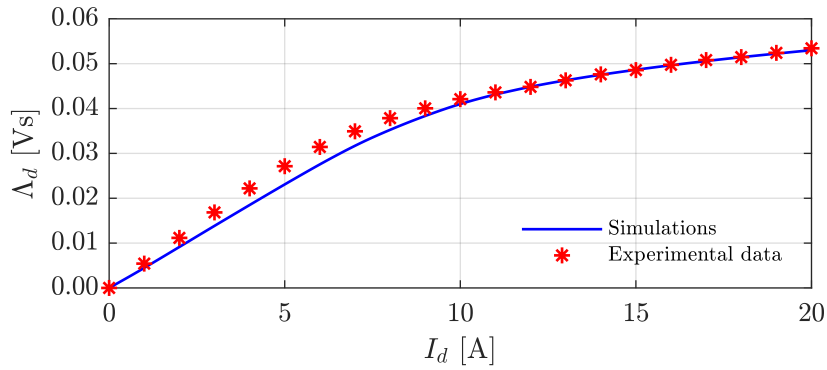

(**a**) Direct flux linkage

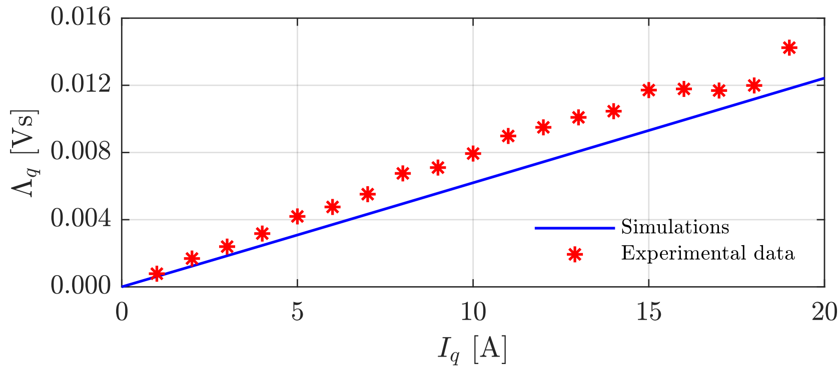

(**b**) Quadrature flux linkage

Figure 13. Comparison between finite element simulations and experimental measurements on the printed rotor.

5. Conclusions

This paper provides a detailed description of the manufacturing process and the magnetic characterization of a toroid realized by additive manufacturing. In particular the BH curve and power losses have been analyzed for different operating frequencies. It is highlighted that the printing process strongly influences the core properties but, thanks to a proper design, magnetic characteristics similar to laminations can be achieved. The realized prototype, in fact, shows a good BH curve and power losses, comparable with those of commercial laminations. The developed magnetic analysis is mandatory for further research in the electric machine field in order to perform accurate simulations which involve electric machines with AM cores. As a real electric motor design example, an AM synchronous reluctance motor is considered. The flux-linkage simulation results have been compared with experimental measurements carried out on a motor prototype.

Author Contributions: Methodology, D.M.; Software, D.M.; Validation, D.M.; Formal analysis, D.M.; Investigation, D.M.; Data curation, D.M.; Writing—original draft, D.M.; Writing—review & editing, D.M., L.A., F.Z. and S.C.; Supervision, L.A. All authors have read and agreed to the published version of the manuscript.

Funding: This project has been funded in the frame of BIRD 2021 call of the Padova University, project id ALBE BIRD2121 01 entitled Design of synchronous reluctance motor for additive manufacturing technology.

Data Availability Statement: Data are contained within the article.

Conflicts of Interest: The authors declare no conflict of interest.

References

1. Lindzen, R.S. Climate Dynamics and Global Change. *Annu. Rev. Fluid Mech.* **1994**, *26*, 353–378. [CrossRef]
2. Drouet, L.; Bosetti, V.; Padoan, S.A.; Aleluia Reis, L.; Bertram, C.; Dalla Longa, F.; Després, J.; Emmerling, J.; Fosse, F.; Fragkiadakis, K.; et al. Net zero-emission pathways reduce the physical and economic risks of climate change. *Nat. Clim. Chang.* **2021**, *11*, 1070–1076. [CrossRef]
3. Davis, S.J.; Lewis, N.S.; Shaner, M.; Aggarwal, S.; Arent, D.; Azevedo, I.L.; Benson, S.M.; Bradley, T.; Brouwer, J.; Chiang, Y.M.; et al. Net-zero emissions energy systems. *Science* **2018**, *360*, eaas9793. [CrossRef] [PubMed]
4. Fankhauser, S.; Smith, S.M.; Allen, M.; Axelsson, K.; Hale, T.; Hepburn, C.; Kendall, J.M.; Khosla, R.; Lezaun, J.; Mitchell-Larson, E.; et al. The meaning of net zero and how to get it right. *Nat. Clim. Chang.* **2021**, *12*, 15–21. [CrossRef]
5. Azevedo, I.; Bataille, C.; Bistline, J.; Clarke, L.; Davis, S. Net-zero emissions energy systems: What we know and do not know. *Energy Clim. Chang.* **2021**, *2*, 100049. [CrossRef]
6. Wong, K.V.; Hernandez, A. A Review of Additive Manufacturing. *ISRN Mech. Eng.* **2012**, *2012*, 208760. [CrossRef]
7. Frazier, W.E. Metal Additive Manufacturing: A Review. *J. Mater. Eng. Perform.* **2014**, *23*, 1917–1928. [CrossRef]
8. Bourell, D.L. Perspectives on Additive Manufacturing. *Annu. Rev. Mater. Res.* **2016**, *46*, 1–18. [CrossRef]
9. Kim, H.; Lin, Y.; Tseng, T.L.B. A review on quality control in additive manufacturing. *Rapid Prototyp. J.* **2018**, *24*, 645–669. [CrossRef]
10. Chen, Z.; Han, C.; Gao, M.; Kandukuri, S.Y.; Zhou, K. A review on qualification and certification for metal additive manufacturing. *Virtual Phys. Prototyp.* **2021**, *17*, 382–405. [CrossRef]
11. Hasanov, S.; Alkunte, S.; Rajeshirke, M.; Gupta, A.; Huseynov, O.; Fidan, I.; Alifui-Segbaya, F.; Rennie, A. Review on Additive Manufacturing of Multi-Material Parts: Progress and Challenges. *J. Manuf. Mater. Process.* **2021**, *6*, 4. [CrossRef]
12. Vafadar, A.; Guzzomi, F.; Rassau, A.; Hayward, K. Advances in Metal Additive Manufacturing: A Review of Common Processes, Industrial Applications, and Current Challenges. *Appl. Sci.* **2021**, *11*, 1213. [CrossRef]
13. Mhetre, G.N.; Jadhav, V.S.; Deshmukh, S.P.; Thakar, C.M. A Review on Additive Manufacturing Technology. *ECS Trans.* **2022**, *107*, 15355–15374. [CrossRef]
14. Wu, Y.; Lu, Y.; Zhao, M.; Bosiakov, S.; Li, L. A Critical Review of Additive Manufacturing Techniques and Associated Biomaterials Used in Bone Tissue Engineering. *Polymers* **2022**, *14*, 2117. [CrossRef]
15. Srivastava, M.; Rathee, S.; Patel, V.; Kumar, A.; Koppad, P.G. A review of various materials for additive manufacturing: Recent trends and processing issues. *J. Mater. Res. Technol.* **2022**, *21*, 2612–2641. [CrossRef]
16. Druzgalski, C.; Ashby, A.; Guss, G.; King, W.; Roehling, T.; Matthews, M. Process optimization of complex geometries using feed forward control for laser powder bed fusion additive manufacturing. *Addit. Manuf.* **2020**, *34*, 101169. [CrossRef]
17. Colosimo, B.M.; Grasso, M.; Garghetti, F.; Rossi, B. Complex geometries in additive manufacturing: A new solution for lattice structure modeling and monitoring. *J. Qual. Technol.* **2021**, *54*, 392–414. [CrossRef]
18. AM, M. Airbus Helicopters Begins High-Volume Metal Additive Manufacturing of A350 Components. Available online: https://www.metal-am.com/airbus-helicopters-begins-large-scale-metal-additive-manufacturing-of-a350-components/ (accessed on 9 January 2024).
19. Metal AM. Boeing 777X Takes Flight with Reported 300 Additively Manufactured Parts in Each GE9X Engine. Available online: https://www.metal-am.com/boeing-777x-takes-flight-with-reported-300-additively-manufactured-parts-in-each-ge9x-engine/ (accessed on 9 January 2024).
20. Simpson, N.; Mellor, P.H. Additive manufacturing of shaped profile windings for minimal AC loss in gapped inductors. In Proceedings of the 2017 IEEE International Electric Machines and Drives Conference (IEMDC), Miami, FL, USA, 21–24 May 2017. [CrossRef]
21. Wohlers, C.; Juris, P.; Kabelac, S.; Ponick, B. Design and direct liquid cooling of tooth-coil windings. *Electr. Eng.* **2018**, *100*, 2299–2308. [CrossRef]
22. Simpson, N.; North, D.J.; Collins, S.M.; Mellor, P.H. Additive Manufacturing of Shaped Profile Windings for Minimal AC Loss in Electrical Machines. *IEEE Trans. Ind. Appl.* **2020**, *56*, 2510–2519. [CrossRef]
23. Compton, B.G.; Kemp, J.W.; Novikov, T.V.; Pack, R.C.; Nlebedim, C.I.; Duty, C.E.; Rios, O.; Paranthaman, M.P. Direct-write 3D printing of NdFeB bonded magnets. *Mater. Manuf. Process.* **2016**, *33*, 109–113. [CrossRef]
24. Paranthaman, M.P.; Shafer, C.S.; Elliott, A.M.; Siddel, D.H.; McGuire, M.A.; Springfield, R.M.; Martin, J.; Fredette, R.; Ormerod, J. Binder Jetting: A Novel NdFeB Bonded Magnet Fabrication Process. *JOM* **2016**, *68*, 1978–1982. [CrossRef]
25. Urban, N.; Huber, F.; Franke, J. Influences of process parameters on rare earth magnets produced by laser beam melting. In Proceedings of the 2017 7th International Electric Drives Production Conference (EDPC), Wuerzburg, Germany, 5–6 December 2017. [CrossRef]
26. Pham, T.; Kwon, P.; Foster, S. Additive Manufacturing and Topology Optimization of Magnetic Materials for Electrical Machines—A Review. *Energies* **2021**, *14*, 283. [CrossRef]
27. Tate, J.; Richardson, B.; Love, L. *Additive Manufacturing for Low Volume Bearings*; USDOE Office of Energy Efficiency and Renewable Energy: Washington, DC, USA, 2017. [CrossRef]
28. Wrobel, R.; Mecrow, B. A Comprehensive Review of Additive Manufacturing in Construction of Electrical Machines. *IEEE Trans. Energy Convers.* **2020**, *35*, 1054–1064. [CrossRef]

29. Cavagnino, A.; Vaschetto, S.; Pošković, E.; Fortunato, A.; Liverani, E. Magnetic Behavior and Loss Assessment of Additively Manufactured Fe-Si alloys. In Proceedings of the 2023 IEEE International Electric Machines & Drives Conference (IEMDC), San Francisco, CA, USA, 15–18 May 2023; pp. 1–6. [CrossRef]
30. Tiismus, H.; Kallaste, A.; Belahcen, A.; Tarraste, M.; Vaimann, T.; Rassõlkin, A.; Asad, B.; Shams Ghahfarokhi, P. AC Magnetic Loss Reduction of SLM Processed Fe-Si for Additive Manufacturing of Electrical Machines. *Energies* **2021**, *14*, 1241. [CrossRef]
31. Pham, T.Q.; Do, T.T.; Kwon, P.; Foster, S.N. Additive Manufacturing of High Performance Ferromagnetic Materials. In Proceedings of the 2018 IEEE Energy Conversion Congress and Exposition (ECCE), Portland, OR, USA, 23–27 September 2018. [CrossRef]
32. Tiismus, H.; Kallaste, A.; Belahcen, A.; Vaimann, T.; Rassõlkin, A.; Lukichev, D. Hysteresis Measurements and Numerical Losses Segregation of Additively Manufactured Silicon Steel for 3D Printing Electrical Machines. *Appl. Sci.* **2020**, *10*, 6515. [CrossRef]
33. Goll, D.; Schuller, D.; Martinek, G.; Kunert, T.; Schurr, J.; Sinz, C.; Schubert, T.; Bernthaler, T.; Riegel, H.; Schneider, G. Additive manufacturing of soft magnetic materials and components. *Addit. Manuf.* **2019**, *27*, 428–439. [CrossRef]
34. Quercio, M.; Galbusera, F.; Poskovic, E.; Franchini, F.; Ferraris, L.; Canova, A.; Gruosso, G.; Demir, A.G.; Previtali, B. Functional characterization of L-PBF produced FeSi2.9 Soft Magnetic Material. In Proceedings of the 2022 International Conference on Electrical Machines (ICEM), Valencia, Spain, 5–8 September 2022. [CrossRef]
35. Tong, C. *Introduction to Materials for Advanced Energy Systems*; Springer International Publishing: Cham, Switzerland, 2019. [CrossRef]
36. Lesuer, D.R.; Syn, C.K.; Sherby, O.D.; Wadsworth, J.; Lewandowski, J.J.; Hunt, W.H. Mechanical behaviour of laminated metal composites. *Int. Mater. Rev.* **1996**, *41*, 169–197. [CrossRef]
37. Moses, A. Electrical steels: Past, present and future developments. *IEEE Proc. A (Phys. Sci. Meas. Instrum. Manag. Educ.)* **1990**, *137*, 233–245. [CrossRef]
38. Bourchas, K.; Stening, A.; Soulard, J.; Broddefalk, A.; Lindenmo, M.; Dahlén, M.; Gyllensten, F. Influence of cutting and welding on magnetic properties of electrical steels. In Proceedings of the 2016 XXII International Conference on Electrical Machines (ICEM), Lausanne, Switzerland, 4–7 September 2016; pp. 1815–1821. [CrossRef]
39. Michieletto, D.; Alberti, L. Design and Realization of a Synchronous Reluctance Motor with Printed Rotor. In Proceedings of the IECON 2022—48th Annual Conference of the IEEE Industrial Electronics Society, Brussels, Belgium, 17–20 October 2022. [CrossRef]
40. Michieletto, D.; Alberti, L. A Scalable Analytical Model for Printed Multi-Barrier Reluctance Rotor. In Proceedings of the 2023 IEEE International Electric Machines & Drives Conference (IEMDC), San Francisco, CA, USA,15–18 May 2023; pp. 1–7. [CrossRef]
41. Michieletto, D.; Alberti, L. On the performance of PMAREL and REL Synchronous Motor Prototypes with Printed Rotor. In Proceedings of the 2023 IEEE Energy Conversion Congress and Exposition (ECCE), Nashville, TN, USA, 29 October–2 November 2023; pp. 3953–3958. [CrossRef]
42. Gibson, I.; Rosen, D.; Stucker, B.; Khorasani, M. *Additive Manufacturing Technologies*; Springer: Cham, Switzerland, 2021.
43. Hossain, M.S.; Gonzalez, J.A.; Hernandez, R.M.; Shuvo, M.A.I.; Mireles, J.; Choudhuri, A.; Lin, Y.; Wicker, R.B. Fabrication of smart parts using powder bed fusion additive manufacturing technology. *Addit. Manuf.* **2016**, *10*, 58–66. [CrossRef]
44. Sun, S.; Brandt, M.; Easton, M. Powder bed fusion processes. In *Laser Additive Manufacturing*; Elsevier: Amsterdam, The Netherlands, 2017; pp. 55–77. [CrossRef]
45. Sisma. MySint100 Datasheet. Available online: https://www.sisma.com/en/products/mysint100/ (accessed on 9 January 2024).
46. Höganäs. Available online: https://www.hoganas.com/en/ (accessed on 9 January 2024).
47. Arató, P.; Bóc, I.; Gróf, T. Effect of composition on the loss of non-oriented medium silicon electric steels. *J. Magn. Magn. Mater.* **1984**, *41*, 53–55. [CrossRef]
48. Hou, C.K. Effect of silicon on the loss separation and permeability of laminated steels. *J. Magn. Magn. Mater.* **1996**, *162*, 280–290. [CrossRef]
49. Shimanaka, H.; Ito, Y.; Matsumara, K.; Fukuda, B. Recent development of non-oriented electrical steel sheets. *J. Magn. Magn. Mater.* **1982**, *26*, 57–64. [CrossRef]
50. Kan, T.; Ito, Y.; Shimanaka, H. Magnetic properties of roller-quenched high silicon steel ribbons. *J. Magn. Magn. Mater.* **1982**, *26*, 127–129. [CrossRef]
51. Nikon. Nikon Metrology MCT225 Datasheet. Available online: https://industry.nikon.com/en-aom/wp-content/uploads/sites/20/2021/11/mct225-en.pdf (accessed on 9 January 2024).
52. King, W.E.; Barth, H.D.; Castillo, V.M.; Gallegos, G.F.; Gibbs, J.W.; Hahn, D.E.; Kamath, C.; Rubenchik, A.M. Observation of keyhole-mode laser melting in laser powder-bed fusion additive manufacturing. *J. Mater. Process. Technol.* **2014**, *214*, 2915–2925. [CrossRef]
53. Wang, L.; Zhang, Y.; Chia, H.Y.; Yan, W. Mechanism of keyhole pore formation in metal additive manufacturing. *npj Comput. Mater.* **2022**, *8*, 22. [CrossRef]
54. Huang, Y.; Fleming, T.G.; Clark, S.J.; Marussi, S.; Fezzaa, K.; Thiyagalingam, J.; Leung, C.L.A.; Lee, P.D. Keyhole fluctuation and pore formation mechanisms during laser powder bed fusion additive manufacturing. *Nat. Commun.* **2022**, *13*, 1170. [CrossRef] [PubMed]
55. Qu, M.; Guo, Q.; Escano, L.I.; Clark, S.J.; Fezzaa, K.; Chen, L. Mitigating keyhole pore formation by nanoparticles during laser powder bed fusion additive manufacturing. *Addit. Manuf. Lett.* **2022**, *3*, 100068. [CrossRef]

56. Mukherjee, T.; Zuback, J.S.; De, A.; DebRoy, T. Printability of alloys for additive manufacturing. *Sci. Rep.* **2016**, *6*, 19717. [CrossRef]
57. Mukherjee, T.; DebRoy, T. Mitigation of lack of fusion defects in powder bed fusion additive manufacturing. *J. Manuf. Process.* **2018**, *36*, 442–449. [CrossRef]
58. Ning, J.; Wang, W.; Zamorano, B.; Liang, S.Y. Analytical modeling of lack-of-fusion porosity in metal additive manufacturing. *Appl. Phys. A* **2019**, *125*, 797. [CrossRef]
59. Bustillos, J.; Kim, J.; Moridi, A. Exploiting lack of fusion defects for microstructural engineering in additive manufacturing. *Addit. Manuf.* **2021**, *48*, 102399. [CrossRef]
60. Wits, W.W.; Carmignato, S.; Zanini, F.; Vaneker, T.H.J. Porosity testing methods for the quality assessment of selective laser melted parts. *CIRP Ann.-Manuf. Technol.* **2016**, *65*, 201–204. [CrossRef]
61. Fiorillo, F. *Characterization and Measurement of Magnetic Materials*; Elsevier: Amsterdam, The Netherlands, 2004. [CrossRef]
62. Voestalpine. Isovac 350-50A Datasheet. 01/2018 Last Updated. Available online: https://www.voestalpine.com/division_stahl/content/download/32782/347314/file/DB_isovac_350-50A_E_280715.pdf, (accessed on 9 January 2024).
63. Meeker, D.; Bianchi, N.; Gyselinck, J.; Sabariego, R.; Alberti, L.; Pellegrino, G.; Cupertino, F. Electrical machine analysis using free software. In Proceedings of the 2017 IEEE Energy Conversion Congress and Exposition (ECCE), Cincinnati, OH, USA, 1–5 October 2017.